Journal of Materials Chemistry A

ROYAL SOCIETY OF CHEMISTRY

PAPER

View Article Online
View Journal | View Issue

Cite this: J. Mater. Chem. A, 2024, 12, 335

Mechanosynthesis of a bifunctional FeNi–N–C oxygen electrocatalyst *via* facile mixed-phase templating and preheating-pyrolysis†

Akmal Kosimov,[a] Gulnara Yusibova,[a] Ivan Tito Wojsiat,[a] Jaan Aruväli,[b] Maike Käärik,[a] Jaan Leis,[a] Peeter Paaver,[b] Sergei Vlassov,[c] Arvo Kikas,[c] Vambola Kisand,[c] Helle-Mai Piirsoo,[c] Kaupo Kukli,[c] Ivo Heinmaa,[d] Tiit Kaljuvee[e] and Nadezda Kongi *[a]

Metal–air batteries (MABs) offer a promising solution to address the intermittent nature of renewable energy sources and facilitate the global transition to green energy, thereby mitigating climate issues. However, efficient and affordable bifunctional electrocatalysts are essential to overcome the kinetic limitations of the oxygen reduction reaction (ORR) and oxygen evolution reaction (OER) in MABs, ensuring optimal performance and accessibility of these devices. This study reports a template-assisted mechanosynthesis of a bifunctional FeNi–N–C electrocatalyst by employing low-cost and sustainable $FeCl_3$, $NiCl_2$, 2,4,6-tri(2-pyridyl)-1,3,5-triazine (TPTZ), melamine and KCl. Facile liquid-assisted grinding was utilized to produce KCl-templated FeNi-TPTZ metal–organic material, enabling template-induced stability of the catalyst. A carefully tailored pyrolysis strategy allows near-melt preheating of FeNi-TPTZ, increasing the concentration of active sites. Furthermore, the pyrolysis protocol enables the phase transition of KCl, functionalizing it as a solid–liquid template to achieve a high porosity (S_{BET} = 570 m^2 g^{-1}). The produced catalyst – IroNi-3D exhibits impressive ORR ($E_{1/2}$ = 0.82 V, E_{onset} = 0.92 V) and OER ($E_{j=10}$ = 1.52 V) performance with a ΔE of 0.70 V. In zinc–air battery testing, IroNi-3D outperforms PtRu with a power density of 144 mW cm^{-2}. This cost-effective FeNi–N–C electrocatalyst presents great promise for widespread use in MABs, advancing renewable energy storage and contributing to global climate change mitigation.

Received 1st August 2023
Accepted 14th November 2023

DOI: 10.1039/d3ta04580c

rsc.li/materials-a

Introduction

The pressing global concern of climate change necessitates a transition to alternative energy sources.[1] However, the reliance of renewable energy sources on external factors (weather conditions, time of day, season, and location) makes it challenging to match supply with demand.[2–4] Thus, the implementation of electrochemical energy storage (EES) systems becomes crucial for effectively storing excess energy and ensuring a reliable and efficient energy supply.[5] In particular, metal–air batteries (MABs) are gaining attention as promising options for storing renewable energy efficiently and at a low cost.[6,7] MABs show remarkable theoretical energy density, which can be 5 to 25 times higher than that of current analogs.[8] MABs, however, are hindered by the kinetics of the two main reactions, the oxygen reduction reaction (ORR) and oxygen evolution reaction (OER). Therefore, great effort has been put into finding a suitable electrocatalyst that can be efficient in both reactions, thus having an optimized bifunctionality as well as having great stability during charge–recharge cycles.[9–11]

The combination of platinum group metal (PGM) catalysts has been reported to exert bifunctional activity and is currently considered the benchmark. However, high costs and low availability make their use unfeasible. In pursuit of a better alternative, metal–nitrogen–doped carbon (M–N–C) catalysts rose as a potential solution, with the metal component typically being cost-effective and widely available transition metals (Fe, Co, Ni, Mn, Zn, *etc.*).[12–14] The carbon matrix in M–N-Cs exhibits excellent conductivity while nitrogen- and metal-based catalytic sites enable bifunctional catalytic activity comparable to that of PGMs.[15] More specifically, pyridinic and graphitic nitrogen species and metal single atom sites are responsible for the efficient ORR activity,[16–18] whereas metal nanoparticles facilitate

[a]Institute of Chemistry, University of Tartu, Ravila 14a, 50411, Tartu, Estonia. E-mail: nadezda.kongi@ut.ee
[b]Institute of Ecology and Earth Sciences, University of Tartu, Ravila 14a, 50411, Tartu, Estonia
[c]Institute of Physics, University of Tartu, Ostwaldi 1, 50411, Tartu, Estonia
[d]National Institute of Chemical Physics and Biophysics (NICPB), Acadeemia tee 23, 12618, Tallinn, Estonia
[e]Department of Materials and Environmental Technology, Tallinn Technical University, Ehitajate tee 5, 19086 Tallinn, Estonia

† Electronic supplementary information (ESI) available. See DOI: https://doi.org/10.1039/d3ta04580c

OER activity.[19,20] In particular, iron-based single-atom catalysts were reported to exhibit an outstanding ORR performance,[21,22] and iron–nickel nanoparticles showed excellent OER performance.[23–27]

Currently, most synthetic methods for M–N–C involve solvent-based approaches (dissolution, hydrothermal/solvothermal, and precipitation), which can often generate a substantial quantity of waste and be material, cost, and energy intensive.[28,29] Therefore, in recent studies, mechanosynthesis has been employed as an effective and greener alternative for conventional solvent-based synthesis to reduce or eliminate the generation of waste and material and energy overuse.[30–33] The mechanochemical synthesis is performed in a solid phase where mechanical energy is transferred to reactants by grinding with minimal or no solvent.[34–36] Furthermore, to advance the solid-phase synthesis of M–N-Cs, templating with cheap and abundant inorganics is employed to boost the catalytic performance and production efficiency. Template-assisted synthesis involves using a scaffold that provides a spatial framework for the desired product once the template is removed to direct the morphology and pore distribution, thereby creating a hierarchical porous structure – a vital characteristic for high-performance catalysts.[29,37] Inorganic compounds (NaCl, KCl, MgO, SiO_2, Al_2O_3, *etc.*) are often used in template-assisted synthesis as inexpensive, stable, environmentally friendly, and easy-to-remove compounds.[38–40] As demonstrated previously, template-induced porosity facilitates superior activities in the ORR/OER compared to their non-templated counterparts.[41,42]

Notably, Fellinger *et al.* reported in their study on nitrogen-doped carbon catalysts that the porosity characteristics of the catalyst are also influenced by the phase of the template,[43] which can be either liquid, solid, or a mixture. In their work, they utilized a template consisting of a combination of $ZnCl_2$ and NaCl, with different template states achieved by varying the NaCl content. Interestingly, the highest porosity ($SSA_{BET} = 2900$ m^2 g^{-1}) was observed when using a eutectic mixture of $ZnCl_2$: NaCl at 33 mol% NaCl. However, the most favorable catalytic activity ($E_{1/2} = 0.880$ V) was achieved using an 80 mol% NaCl template, which undergoes a phase transition from a mixed phase to a salt melt at higher temperatures (>650 °C). The study revealed that although the mixed phase induced by higher NaCl content, reduced the porosity it resulted in increased mesopore size and additional macropores, ultimately leading to a fine pore structure associated with high catalytic activity. Inspired by these findings, our work aims to leverage phase-induced porosity using a single-component template while incorporating iron-and-nickel-based active sites to achieve a high bifunctional activity.

Herein, we present a template-assisted mechanosynthesis protocol for bi-metallic M–N-Cs for zinc–air batteries. The synthesis method prioritizes eco-friendly, inexpensive materials ($FeCl_3$, $NiCl_2$, TPTZ, melamine, and KCl) and implements only water as a solvent. The synthesis process is based on a technique called liquid-assisted grinding (LAG), utilizing KCl as an abundant and sustainable mixed-phase template. The intrinsic properties of KCl enable its retention as a solid template at 760 °C, facilitating the formation of macro and mesopores, and at a higher temperature of 800 °C, KCl undergoes a phase transition to a liquid state, facilitating the efficient formation of micropores. The described approach yielded a highly porous ($S_{BET} = 570$ m^2 g^{-1}) and efficient bifunctional ORR/OER electrocatalyst – IroNi-3D, which exhibits notable catalytic activity in the ORR ($E_{1/2} = 0.82$ V, $E_{onset} = 0.92$ V) and OER ($E_{j=10} = 1.52$ V). Furthermore, in the Zn–air battery test, IroNi-3D outperformed its commercially available counterparts, achieving a power density of 135 mW cm^{-2} compared to 101 mW cm^{-2} for PtRu. This study addresses the challenges associated with the development of advanced yet feasible synthesis methods for highly efficient M–N-Cs. The findings of this research have significant implications for the scalable, sustainable, and energy/time-efficient production of oxygen electrocatalysts, thus contributing to the advancement of metal–air battery technology.

Results and discussion

Synthesis

In this work, three different FeNi–N–C catalysts were prepared: IroNi-1, IroNi-2, and IroNi-3D, where 3D identifies the application of the templating agent. IroNi-3D was prepared *via* one-step template-assisted mechanosynthesis to yield a FeNi-TPTZ coordination complex supported on a KCl template (FeNi-TPTZ@KCl). The composite was subjected to heat treatment and template removal to produce highly porous FeNi–N–C (Fig. 1). Non-templated IroNi-2 was prepared for comparison to determine the effect of the template. And the non-templated and non-melamine doped catalyst IroNi-2 was prepared to ascertain the benefits of templating and melamine doping. In this study, 2,4,6-tri(2-pyridyl)-1,3,5-triazine (TPTZ) was chosen as the primary ligand and nitrogen/carbon source, supplemented by 2,4,6-triamino-1,3,5-triazine (melamine) to potentially fill any remaining coordination sites and provide additional nitrogen and carbon. In a coordinated state, iron and nickel cations are less prone to clustering during pyrolysis and more likely to stay as single-atom species.[44,45] The preheating of FeNi-TPTZ@KCl conducted at the near melting point of the complex (300 °C) was undertaken to improve the coordination efficiency and single-atom site formation.[22] To enhance

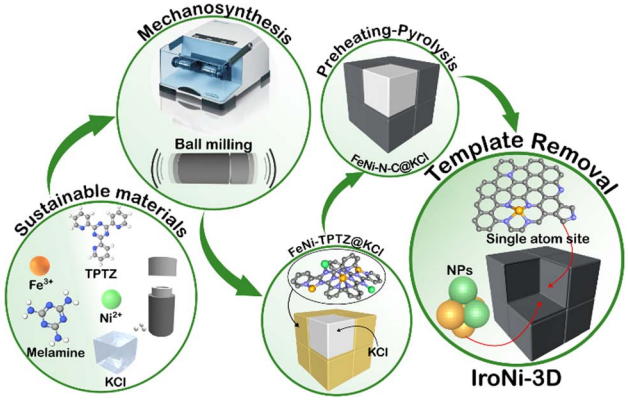

Fig. 1 Schematic illustration of the template-assisted mechanosynthesis process.

complex pyrolysis stability and improve porosity and the concentration of active sites, a KCl-template was incorporated *via* liquid-assisted grinding.[45] Apart from acting as a grinding aid,[46] KCl acts as a salt-melt – highly polar solvent,[47] allowing metal cations to coordinate with nitrogen species more effectively. In the developed mixed-phase templating and near-melting point preheating approach, a precise pyrolysis strategy is of key importance. The preheating temperature for FeNi-TPTZ was established by thermogravimetric analysis, which shows that 300 °C is the upper limit of non-destructive heating (Fig. S1a†). To achieve the phase transition of the template from solid to liquid, the temperature must be higher than the melting point of KCl (760 °C). Thus, the pyrolysis strategy was designed as gradual heating (10 °C min^{-1}) with 1 hour dwellings at 300 °C and 800 °C (Fig. S1b†). As opposed to conventional acid leaching,[48] hydrothermal treatment was implemented in this work to remove the KCl template and ensure the enrichment of the carbon matrix with active metal species.

Characterization

After the mechanochemical treatment, a color shift was observed, transitioning from a pale yellow to dark green. This alteration in color serves as a preliminary confirmation of the structural modification (Fig. S2a†), which was further corroborated through comparative PXRD analysis (Fig. S2b†), where the formed FeNi-TPTZ pattern does not resemble the patterns of the starting reactants. FeNi-TPTZ was recrystallized as needle-like green crystals (Fig. S2c†), and characteristic coordination peaks were identified by comparative solid-state NMR (Fig. 2d), where the Fe–Ni-TPTZ MAS-NMR spectrum at fast spinning showed peaks of Fe-TPTZ (328, 231, 220, 199, 92, and 32 ppm) and the characteristic peaks of the Ni-TPTZ spectrum (516, 327, 194, and 93 ppm), affirming the formation of an Fe and Ni-coordinated TPTZ complex. With the template, the microscopy images (Fig. 2a and b) reveal the homogeneous incorporation of KCl into FeNi-TPTZ. This inclusion of KCl is vital as it plays a pivotal role in stabilizing the FeNi-TPTZ complex during pyrolysis, ultimately leading to enhanced porosity and increased exposure to catalytically active sites. Upon hydrothermal washing, the microscopy image of IroNi-3D (Fig. 2c) demonstrates the creation of a porous open-frame 3D structure induced by the template. SEM images of IroNi-3D confirm the detected porosity of the material, showing an open carbon matrix with a large variety of pores (Fig. 2d) and enhanced exposure of the carbon surface and OER-active FeNi nanoparticles (Fig. 2e), which are mainly distributed over the range of 10–30 nm (Fig. 2f). On the other hand, IroNi-2 presents closely packed carbon agglomerates (Fig. S3a†), which wrap around the FeNi nanoparticles (Fig. S3b†) with an average size of 20–60 nm (Fig. S3c†). Lastly, template and melamine-free IroNi-1 presents a dense carbon matrix (Fig. S4d†) with the inclusion of FeNi nanoparticles (Fig. S3e†) with sizes spanning in the range of 20–140 nm (Fig. S4f†). In IroNi-2 and IroNi-1, the absence of a template resulted in a larger and non-homogenous distribution of agglomerate sizes, demonstrating the importance of KCl templating in forming evenly distributed and well-exposed nanoparticles. The nitrogen gas adsorption and desorption analysis results supported the template-promoted enhancement in porosity. The produced FeNi–N–C materials exhibit a type IV hysteresis loop shape in the adsorption–desorption isotherms (Fig. 2g (inset)), containing both micro- and mesopores distributed over the range of 1.2–2 nm and 2.5–5 nm, respectively (Fig. 2g). Among the samples, the templated IroNi-3D showed a great porosity of $S_{BET} = 570\ m^2\ g^{-1}$, whereas IroNi-2 and IroNi-1 demonstrate a surface area of 208 and 284 $m^2\ g^{-1}$, respectively (Table S1†). Additionally, IroNi-3D demonstrated a significantly greater surface area of mesopores (194 $m^2\ g^{-1}$) and micropores (288 $m^2\ g^{-1}$) compared to non-templated catalysts (Table S1,† and Fig. 2h). A high volume of micro-and mesopores in IroNi-3D hints at improved kinetics, as they are crucial for efficient mass and charge transfer.[49]

Powder X-ray diffraction (PXRD) analysis was performed to determine the composition and crystalline characteristics of the samples after hydrothermal washing (Fig. 3a). All IroNi catalysts exhibited five distinct peaks corresponding to the hexagonal graphitic structure (graphite-2H; 26°)[50] and the cubic FeNi alloy (taenite; 43.5°, 50.5°, 74.5°, and 91°).[23] Notably, the templated IroNi-3D additionally displayed small peaks of Fe_3O_4, which could be a result of minor oxidation during hydrothermal treatment due to better exposure of the particles in IroNi-3D. Overall, the PXRD data demonstrate that the developed templating method is effective in forming abundant OER-active FeNi nanoparticles, which are scattered on the surface of a porous carbon matrix due to improved ion mobility in a salt melt of the KCl template.

Furthermore, the surface atomic composition of the catalysts was analyzed with X-ray photoelectron spectroscopy (XPS). The surface of all the catalysts contains C, N, O, Fe, and Ni atoms (Fig. S4†). Deconvoluted N 1s spectra show that the material is abundant in active nitrogen species (Fig. 3b) (graphitic – 401.62 eV, pyrrolic – 400.5 eV, and pyridinic – 398.4 eV) and nitrogen-coordinated metal sites (M–N_x – 399.38 eV), which contain over 80% of all surface nitrogen atoms (Fig. 3c). The confirmation of the presence of single-atom sites through XPS analysis is further supported by the HAADF-STEM elemental mapping (Fig. S13†), where the spots lacked discernible boundaries/edges, and EDX analysis revealed elevated levels of Fe and Ni in these regions, potentially indicating a dense concentration of single-atom sites. All three samples show a somewhat similar concentration of M–N_x sites (Fig. 3c), which are responsible for an effective ORR. However, as was demonstrated in our previous studies, a lack of porosity will lead to a lowered electrochemical activity due to poor exposure to catalytically active sites.[29] The C 1s spectrum (Fig. S5a†) displays characteristic peaks at 284.5 and 284.8 eV that can be ascribed to the sp 2 and sp 3 carbons, respectively.[51] Both C 1s and O 1s spectra (Fig. S5a and b†) show the peaks of oxygen-containing functional groups in all IroNi catalysts. The low oxidation degree shows good carbon quality, which is in good agreement with C 1s analysis. Furthermore, the O 1s spectrum shows a distinct peak located at 529.7, corresponding to metal oxide, which can be attributed to the presence of Fe_3O_4 in the

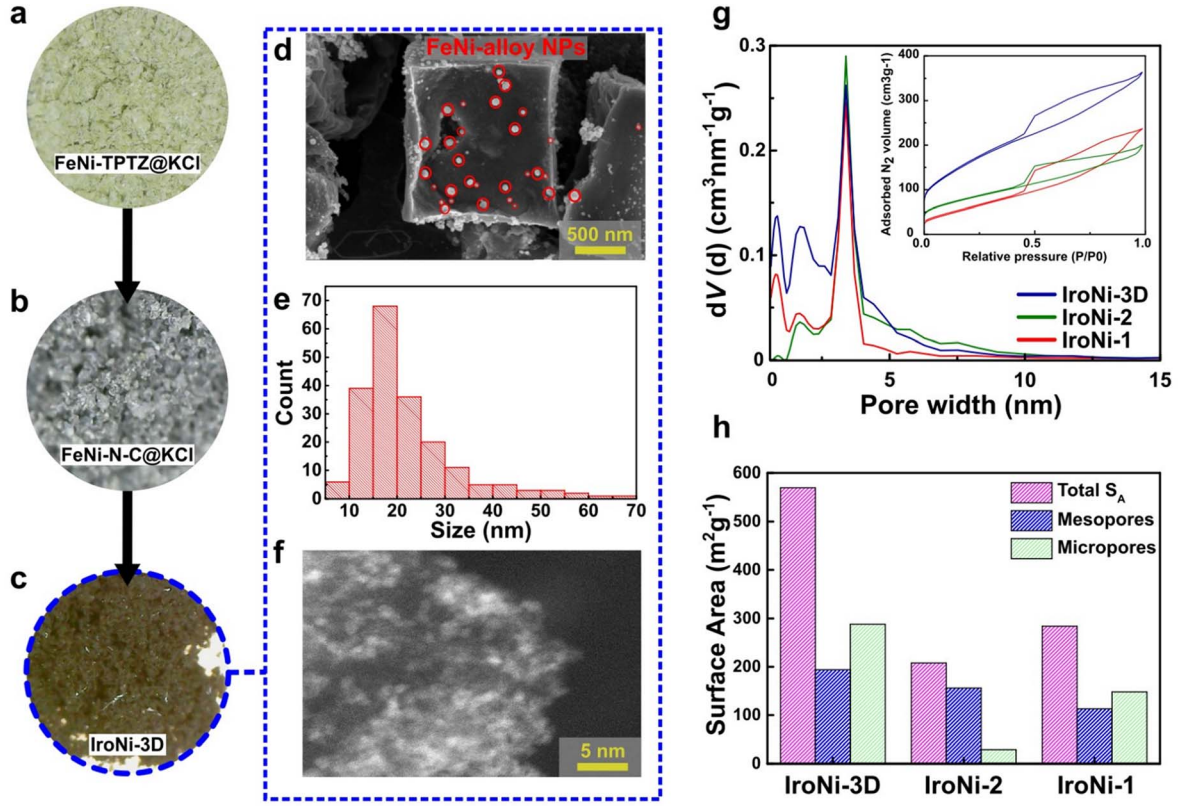

Fig. 2 (a–c) IroNi-3d at different processing stages; (d) SEM image of IroNi-3d; (e) particle size distribution of FeNi nanoparticles in IroNi-3d; (f) HR-STEM image of IroNi-3d; (g) pore size distribution curves and nitrogen adsorption–desorption isotherms (inset). (h) Pore surface area ratio in all three samples.

material.[52] The Fe 2p XPS spectrum (Fig. 3b) shows the peaks of bivalent iron (Fe^{2+}) located at 710.5 eV and 723.7 eV, and the peaks at 712.2 and 725.5 eV attributed to trivalent iron (Fe^{3+}), while the peak at 705.0 eV is assigned to metallic iron (Fe^{0}).[53] All three materials have a satellite peak at around 716 eV, indicating the presence of both Fe^{2+} and Fe^{3+} in all samples.[59] However, in the case of the IroNi sample, this peak has a lower intensity. The high-resolution XPS spectrum of Ni 2p exhibits two spin–orbit peaks at 855.8 eV(Ni $2p_{3/2}$) and 873.4 eV (Ni $2p_{1/2}$) along with two satellite peaks, which can be attributed to Ni II, confirming the effective formation of $FeNi_3$ alloy nanoparticles. Overall, IroNi-3D possesses the lowest surface C and N atomic

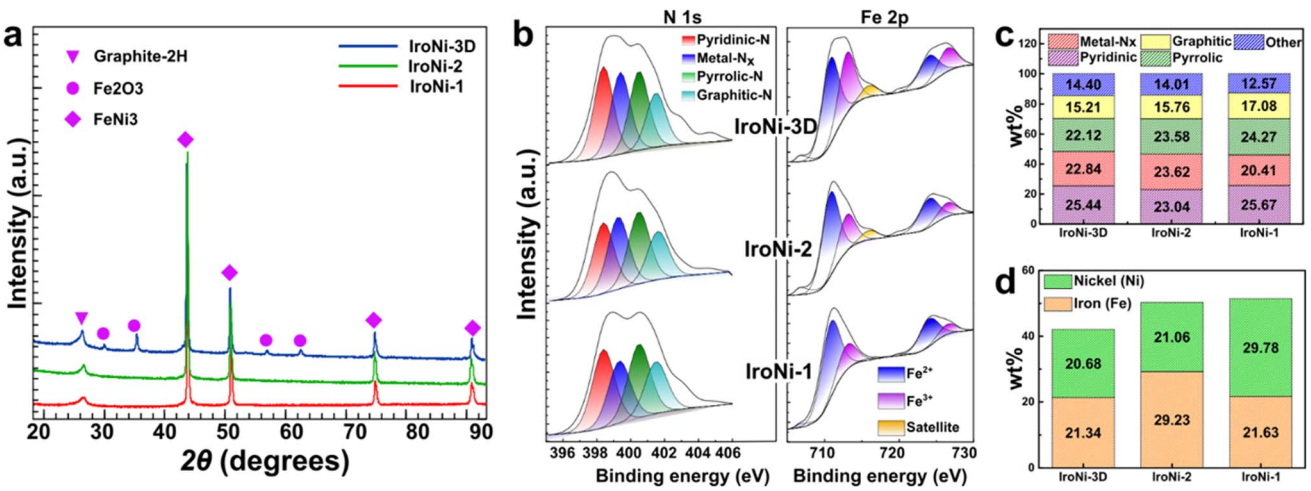

Fig. 3 (a) XRD patterns of the samples IroNi-3d, IroNi-2, and IroNi-1. (b) Deconvoluted high-resolution N 1s and Fe 2p photoelectron spectra of FeNi–N–C catalysts. (c) Distribution of nitrogen species in FeNi–N–C materials. (d) Bulk metal concentration in FeNi–N–C catalysts.

content (52.6 and 2.4 at%, respectively) and the highest Fe and Ni content (2.3 and 14.3 at%, respectively, which suggests a high surface exposure of metal species (Table S2†)). The bulk metal composition of IroNi-3D differs significantly from its surface composition. In bulk, both Fe and Ni content exceeds 20 wt%, and their ratio is nearly 1 : 1 (see Fig. 3d and Table S2†), indicating the successful formation of $FeNi_3$ nanoparticles. However, this results in a reduced surface concentration of M–N_x sites. Furthermore, the metal composition of IroNi-2 has 8% more Fe, whereas, in IroNi-1, there is 8 wt% more Ni. It is suggested that such a discrepancy is caused by the ligands involved in the synthesis, *i.e.*, TPTZ and melamine in IroNi-3D and IroNi-2 created sufficient coordination sites for Fe-ions to be turned into M–N_x, as demonstrated by XPS (Fig. 3c), while Ni in IroNi-1 is retained as large FeNi-agglomerates.

Electrochemical characterization

The performance of the catalysts was assessed through a comprehensive set of tests aimed at understanding the impact of their structural properties and composition on their electrochemical activity. To evaluate the oxygen reduction reaction activity in an alkaline medium (0.1 M KOH), we conducted rotating disk electrode (RDE) studies on the prepared FeNi–N–C samples. The ORR RDE polarization curves (Fig. 4a) demonstrated that IroNi-3D exhibited superior ORR activity. This was evidenced by its higher onset potential (E_{onset} = 0.92 V), half-wave potential ($E_{1/2}$ = 0.82 V), and larger limited current density (5.0 mA cm^{-2}) compared to those of IroNi-2, IroNi-1, and Pt/C, indicating improved electron and mass transfer resulting from its higher porosity.[54,55] Koutecký–Levich (K–L) analysis was further employed to determine the number of electrons (n) transferred per O_2 molecule. As presented in Table S3,† the calculated n values were slightly lower than 4 for all three catalysts in this study. This can be ascribed to the synergistic interplay of individual and combined ORR-active sites, where hydrogen peroxide is first formed and further reduced to water.[58] To evaluate the ORR mechanistic pathway on the prepared materials, Tafel plots were constructed using RDE polarization data (Fig. S9†), and the calculated Tafel slope values are summarized in Table S3.† Among the three catalysts studied, IroNi-3D exhibited the smallest Tafel slope value of around −53 mV dec^{-1}, indicating fast electron transfer followed by a slower chemical step.[58,61] This suggests that IroNi-3D possesses higher ORR activity than IroNi-1 and IroNi-2, as its Tafel slope values are closer to −60 mV dec^{-1}. In order to assess their catalytic performance in the oxygen evolution reaction, the synthesized materials underwent linear sweep voltammetry (LSV) measurements in a 0.1 M KOH solution in an argon-saturated environment with an electrode rotation rate of 1600 rpm. The electrodes were scanned within a potential range of 1.1 to 1.8 V *vs.* RHE to determine the potential required to achieve a current density of 10 mA cm^{-2} ($E_{j=10}$). Fig. 4b illustrates the *iR*-corrected LSV curves, indicating that all the catalysts exhibited an outstanding $E_{j=10}$ value, with the best being IroNi-2 (1.48 V), closely followed by IroNi-1 and IroNi-3D (1.51 V and 1.52 V, respectively). This superior performance was attributed to the abundance of highly OER-active FeNi nanoparticles on the electrode surface.[26,56,57] Moreover, the enhanced performance of the OER in IroNi-2 and IroNi-1 can be attributed to a greater bulk metal composition within the system, as demonstrated by SEM and MP-AES.

Evaluating the OER performance involved the analysis of the Tafel plots. The Tafel plot slope for IroNi-2 exhibited a significantly lower value of 79 mV dec^{-1} (as shown in Fig. S9b†), in stark contrast to the values determined for IroNi-3D (185 mV dec^{-1}) and IroNi-1 (172 mV dec^{-1}). A lower Tafel slope value indicates superior OER efficiency, correlating with a reduced overpotential requirement for the reaction.

To evaluate the bifunctional activity of the prepared electrocatalysts, the value of ΔE (the difference between $E_{j=10}$ and $E_{1/2}$) was used. Fig. 4c presents the results, demonstrating that the IroNi-3D catalyst showcased the lowest ΔE value of 0.70 V, followed by IroNi-2 with a value of 0.71 V. The obtained kinetic parameters for the ORR and OER for all three samples are summarized in Table S3.† The results demonstrate that the efficiency of IroNi-3D is comparable to that of previously reported FeNi–N–C catalysts, as seen in Table S4.† However, it is essential to note that the previously reported liquid-phase protocols fall far behind in cost, energy efficiency, and overall sustainability compared to the proposed solid-phase synthesis approach. The morphological analysis highlights the crucial role of material porosity and the density of active sites in determining the efficient bifunctionality of IroNi-3D. The lower bifunctional activity observed in IroNi-2 and IroNi-1 can be attributed to their lower porosity, which hinders the wetting of the total surface and leads to the inaccessibility and inactivity of a significant portion of active sites.[29] Comparatively, the efficiency of IroNi-3D is found to be on par with that of previously reported FeNi–N–C catalysts (Table S4†), while maintaining the sustainability and cost/energy-efficiency benefits of solid-state synthesis.[28,29]

The bifunctional IroNi-3D catalyst underwent extensive long-term stability testing under ORR and OER conditions. The ORR tests involved prolonged potential cycling of the electrodes in an O_2-saturated electrolyte in the range of 0.6–1.0 V *vs.* RHE (Fig. S10†). For OER stability testing, chronoamperometry was conducted, maintaining the potential at 1.6 V *vs.* RHE continuously for 24 hours. FeNi-3D demonstrated outstanding stability under ORR conditions, as evidenced by the significant overlap of two polarization curves before and after 5000 CV cycles, as depicted in Fig. S10a.† Moreover, during a 24-hour chronoamperometry test at 1.6 V under OER conditions, the catalyst exhibited moderate steady-state stability (Fig. S10b†). Over 24 hours, the current density of FeNi-3D catalysts showed an initial increase. This can be attributed to the development of more active species, including metal hydroxides and oxyhydroxides, as well as the gradual penetration of the electrolyte into the porous structure.[60]

To assess the structure and morphology of the IroNi-3D catalyst after extended stability testing, SEM and EDX analysis were employed. SEM images showed no significant changes in morphology for the FeNi-3D catalyst before and after the stability tests, indicative of its structural stability (Fig. S10 and S11†).

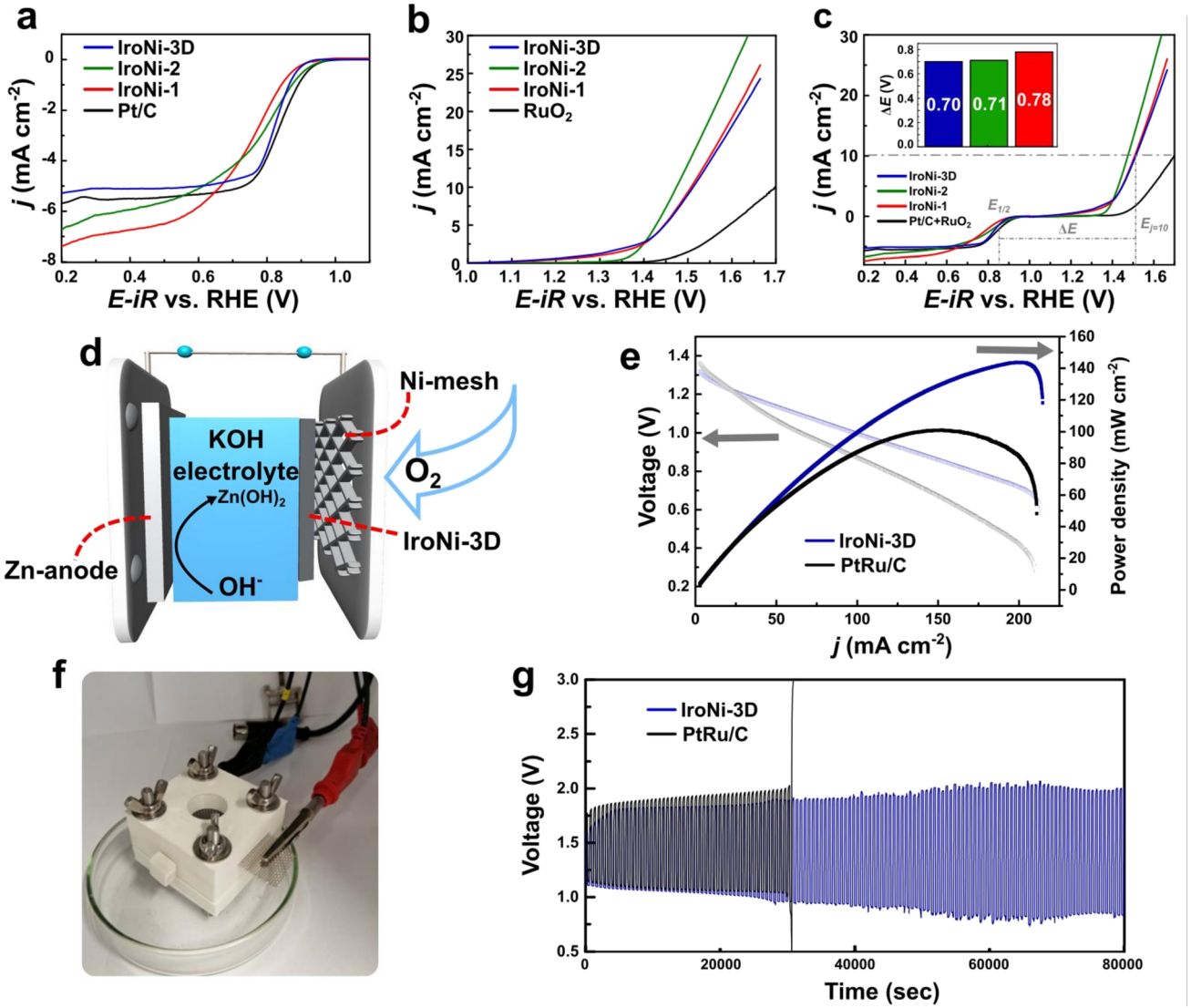

Fig. 4 (a) ORR polarization curves of IroNi-3d, IroNi-2, IroNi-1, and Pt/C in O_2-saturated 0.1 M KOH solution at a rotation rate of 1600 rpm. (b) OER polarization curves of IroNi-3d, IroNi-2, IroNi-1, and RuO_2 in Ar-saturated 0.1 M KOH solution at a rotation rate of 1600 rpm. (c) The overall polarization curves of IroNi-3d, IroNi-2, IroNi-1, and Pt-RuO_2 within the ORR and OER potential window and the values of δ_e (c, inset). (d) Schematic illustration of a zinc–air battery. (e) Power density curves obtained for IroNi-3d and Pt-RuO_2 as catalysts on the air cathode (solid lines – power curves and hollow lines – polarization curves). (f) A photograph of the assembled zinc–air battery. (g) Galvanostatic charging/discharging cycling curves for IroNi-3d and Pt-RuO_2 materials (blue and black lines, respectively) performed at 5 mA cm^{-2}.

Due to an exceptional bifunctional activity, IroNi-3D was selected for further application in the in-house Zn–air battery, which was constructed as a series of stacked plates, where the air cathode represents carbon paper-supported catalysts (Fig. 4d and f). As expected, IroNi-3D demonstrated outstanding performance, showing the highest power density of 144 mW cm^{-2} at 201 mA cm^{-2} (Fig. 4e), comparable to the recent reports (Table S5†). Furthermore, IroNi-3D exhibited superior discharging performance, outperforming PtRu/C, which reached only 101 mW cm^{-2} at 153 mA cm^{-2}. The charge–discharge polarization curve demonstrated that IroNi-3D exhibits an open-circuit voltage of 1.30 V, comparable to that of the PGM-based reference material – PtRu/C (1.35 V). Finally, the long-term performance of IroNi-3D at the air cathode was evaluated through galvanostatic charge–discharge cycling at a current density of 5 mA cm^{-2} (Fig. 4g). In the stability test, the IroNi-3D-driven battery demonstrated a steady voltage–time profile without significant fluctuations for over 22 hours operating in the range of 0.75–1.75 V. Formation of zinc dendrites was suggested to be a reason for the minor fluctuations, which lead to internal short circuits and overall battery instability. Strategies to overcome this shall be examined in separate research. In contrast, the PtRu/C catalyst started to malfunction after only 8 hours of work. The voltage gap of the ZAB with IroNi-3D changed after the charging-discharging cycling stability test and increased from 0.46 to 1.08 V (Fig. S6a and b†). In contrast, the ZAB with PtRu shows a narrower voltage gap, which increased from 0.59 to 0.83 V (Fig. S6c and d†). However,

after ~8 hours, the PtRu ZAB gets completely destabilized, reaching 3 V. The superior stability of IroNi-3D while maintaining decent activity can be attributed to the bifunctional activity of the material. Nevertheless, battery performance heavily depends on the battery assembly and shall be discussed in a separate study. Nonetheless, the results demonstrate the potential application of FeNi–N–C catalysts synthesized through the suggested sustainable solid-state approach.

Conclusions

In this work, we present an original solid-phase synthesis strategy for a FeNi–N–C catalyst that is both sustainable and affordable. The proposed approach yields highly porous Fe/Ni/N-doped carbon materials with excellent bifunctional activity by combining template-assisted mechanosynthesis and a KCl mixed-phase template. While mechanosynthesis provides facile and time and energy-efficient production, the simple temperature-induced mixed-phase templating improves porosity and active site concentration. The outstanding electrochemical activity of IroNi-3D towards the ORR ($E_{1/2}$ = 0.82 V, E_{onset} = 0.92 V) and OER ($E_{j=10}$ = 1.51 V) and exceptional bifunctionality (ΔE = 0.70 V) are attributed to approach-promoted high porosity (S_{BET} = 570 $m^2\ g^{-1}$) and high concentration of ORR/OER active sites (M–N_x/FeNi-nanoparticles). The remarkable bifunctional activity resulted in the IroNi-3D demonstrating promising activity in ZABs (144 mW cm^{-2} at 201 mA cm^{-2}), which can be further improved by tuning the device parameters. Considering the significance of sustainable energy in fostering a more eco-friendly future, the suggested template-assisted mechanosynthesis provides an economically viable and environmentally sustainable approach for fabricating catalysts for metal–air batteries.

Author contributions

A. K. conceived and designed the study. I. T. W. provided the samples for the study. G. Y. and I. T. W. performed the electrochemical experiments and analysed the data. J. L. and M. K. performed the N_2 physisorption experiments and analysed the data. J. A. performed the XRD experiments. A. K. and V. K. performed the XPS experiments and analysed the data. P. P. performed the ICP-AES measurements and analysed the data. S. V., H.-M. P. and K. K. performed SEM and TEM analysis. I. H. performed solid-state NMR and T. K. performed TGA. N. K. supervised the work and revised the manuscript. All authors contributed to the general discussion.

Conflicts of interest

There are no conflicts to declare.

Acknowledgements

The present work was financially supported by the Estonian Research Council (grants PSG250, PRG753, PRG1509, and PRG1702). This research was also supported by the EU through the European Regional Development Fund (TK141, "Advanced materials and high-technology devices for energy recuperation systems"). The authors express their appreciation to Dr Heiki Erikson for his contributions in the design and 3D printing of the Zn–air battery.

References

1 A. I. Osman, L. Chen, M. Yang, G. Msigwa, M. Farghali, S. Fawzy, D. W. Rooney and P.-S. Yap, *Environ. Chem. Lett.*, 2023, **21**, 741–764.
2 W. Zhou, C. J. Cleaver, C. F. Dunant, J. M. Allwood and J. Lin, *Renewable Sustainable Energy Rev.*, 2023, **173**, 113074.
3 N. Li, Z. Lukszo and J. Schmitz, *Renewable Sustainable Energy Rev.*, 2023, **181**, 113308.
4 M. S. Reza, M. A. Hannan, P. J. Ker, M. Mansor, M. S. H. Lipu, M. J. Hossain and T. M. I. Mahlia, *J. Energy Storage*, 2023, **68**, 107698.
5 R. Sharma, H. Kumar, G. Kumar, S. Sharma, R. Aneja, A. K. Sharma, R. Kumar and P. Kumar, *Chem. Eng. J.*, 2023, **468**, 143706.
6 P. Zhang, K. Chen, J. Li, M. Wang, M. Li, Y. Liu and Y. Pan, *Adv. Mater.*, 2023, **35**, 2303243.
7 W. Shao, R. Yan, M. Zhou, L. Ma, C. Roth, T. Ma, S. Cao, C. Cheng, B. Yin and S. Li, *Electrochem. Energy Rev.*, 2023, **6**, 11.
8 S. Hu and M. Zhu, *Curr. Opin. Chem. Eng.*, 2023, **41**, 100926.
9 Y. Zhou, Y. Liu, Z. Wang, C. Li, Z. Wang, S. Zhang and C. Deng, *Energy Storage Mater.*, 2023, **59**, 102772.
10 R. Cepitis, N. Kongi, V. Grozovski, V. Ivanistsev and E. Lust, *Catalysts*, 2021, **11**, 1165.
11 R. Cepitis, N. Kongi, J. Rossmeisl and V. Ivaništšev, *ACS Energy Lett.*, 2023, **8**, 1330–1335.
12 C. Mi, H. Yu, L. Han, L. Zhang, L. Zhai, X. Li, Y. Liu and Z. Xiang, *Adv. Funct. Mater.*, 2023, **33**, 2303235.
13 K. Ping, M. Alam, S. R. Kahnert, R. Bhadoria, A. Mere, V. Mikli, M. Käärik, J. Aruväli, P. Paiste, A. Kikas, V. Kisand, I. Järving, J. Leis, N. Kongi and P. Starkov, *Mater. Adv.*, 2021, **2**, 4009–4015.
14 G. Yusibova, J.-M. Assafrei, K. Ping, J. Aruväli, P. Paiste, M. Käärik, J. Leis, H.-M. Piirsoo, A. Tamm, A. Kikas, V. Kisand, P. Starkov and N. Kongi, *J. Electroanal. Chem.*, 2023, **930**, 117161.
15 S. Chandrasekaran, R. Hu, L. Yao, L. Sui, Y. Liu, A. Abdelkader, Y. Li, X. Ren and L. Deng, *Nano-Micro Lett.*, 2023, **15**, 48.
16 L. Wu, B. Ni, R. Chen, P. Sun and T. Chen, *J. Mater. Chem. A*, 2020, **8**, 21026–21035.
17 S. Akula, M. Mooste, J. Kozlova, M. Käärik, A. Treshchalov, A. Kikas, V. Kisand, J. Aruväli, P. Paiste, A. Tamm, J. Leis and K. Tammeveski, *Chem. Eng. J.*, 2023, **458**, 141468.
18 K. Muuli, A. Sokka, M. Mooste, J. Lilloja, V. Gudkova, M. Käärik, M. Otsus, A. Kikas, V. Kisand, A. Tamm, J. Leis, A. Krumme, S. Holdcroft, J. H. Zagal and K. Tammeveski, *J. Catal.*, 2023, **422**, 117–130.
19 N. Kazimova, K. Ping, M. Alam, M. Danilson, M. Merisalu, J. Aruväli, P. Paiste, M. Käärik, V. Mikli, J. Leis,

K. Tammeveski, P. Starkov and N. Kongi, *J. Catal.*, 2021, **395**, 178–187.
20 Y. Kumar, M. Mooste and K. Tammeveski, *Curr. Opin. Electrochem.*, 2023, **38**, 101229.
21 G. Chen, P. Liu, Z. Liao, F. Sun, Y. He, H. Zhong, T. Zhang, E. Zschech, M. Chen, G. Wu, J. Zhang and X. Feng, *Adv. Mater.*, 2020, **32**, 1907399.
22 C. Ouyang, L. Zheng, Q. Zhang and X. Wang, *Adv. Mater.*, 2022, **34**, 2205372.
23 X. Zhao, P. Pachfule, S. Li, J. R. J. Simke, J. Schmidt and A. Thomas, *Angew. Chem., Int. Ed.*, 2018, **57**, 8921–8926.
24 C. Zhang, C. Wu, Y. Gao, Y. Gong, H. Liu and J. He, *Chem. – Asian J.*, 2021, **16**, 1592–1602.
25 X. Zhang, Y. Chen, B. Wang, M. Chen, B. Yu, X. Wang, W. Zhang and D. Yang, *Electrochim. Acta*, 2019, **321**, 134720.
26 X. Gu, Z. Liu, M. Li, J. Tian and L. Feng, *Appl. Catal., B*, 2021, **297**, 120462.
27 D. Li, H. Liu and L. Feng, *Energy Fuels*, 2020, **34**, 13491–13522.
28 A. Kosimov, G. Yusibova, J. Aruväli, P. Paiste, M. Käärik, J. Leis, A. Kikas, V. Kisand, K. Šmits and N. Kongi, *Green Chem.*, 2022, **24**, 305–314.
29 A. Kosimov, A. Alimbekova, J.-M. Assafrei, G. Yusibova, J. Aruväli, M. Käärik, J. Leis, P. Paiste, M. Ahmadi, K. Roohi, P. Taheri, S. M. Pinto, R. Cepitis, A. J. Baptista, P. Teppor, E. Lust and N. Kongi, *ACS Sustainable Chem. Eng.*, 2023, **11**, 10825–10834.
30 J. Yan, K. Zeng, W. Hu, J. Zhou, X. Chen, C. Wei, R. G. Mendes, M. H. Rümmeli and R. Yang, *ACS Sustainable Chem. Eng.*, 2022, **10**, 7553–7563.
31 M. Gernhard, M. Rautenberg, G. Hörner, B. Weber, F. Emmerling and C. Roth, *Z. Anorg. Allg. Chem.*, 2021, **647**, 2080–2087.
32 H. Li, F. Pan, C. Qin, T. Wang and K.-J. Chen, *Adv. Energy Mater.*, 2023, **13**, 2301378.
33 A. Serov, K. Artyushkova, N. I. Andersen, S. Stariha and P. Atanassov, *Electrochim. Acta*, 2015, **179**, 154–160.
34 A. P. Amrute, J. De Bellis, M. Felderhoff and F. Schüth, *Chem. – Eur. J.*, 2021, **27**, 6819–6847.
35 S. L. James, C. J. Adams, C. Bolm, D. Braga, P. Collier, T. Friščić, F. Grepioni, K. D. M. Harris, G. Hyett, W. Jones, A. Krebs, J. Mack, L. Maini, A. G. Orpen, I. P. Parkin, W. C. Shearouse, J. W. Steed and D. C. Waddell, *Chem. Soc. Rev.*, 2012, **41**, 413–447.
36 J.-L. Do and T. Friščić, *ACS Cent. Sci.*, 2017, **3**, 13–19.
37 Y. Huang, C. An, Q. Zhang, L. Zang, H. Shao, Y. Liu, Y. Zhang, H. Yuan, C. Wang and Y. Wang, *Nano Energy*, 2021, **80**, 105535.
38 F. Sun, T. Liu, M. Huang and L. Guan, *Sustainable Energy Fuels*, 2023, **7**, 3675–3683.
39 T. Friščić, C. Mottillo and H. M. Titi, *Angew. Chem.*, 2020, **132**, 1030–1041.
40 Y. Yang, Y. Yang, Z. Pei, K.-H. Wu, C. Tan, H. Wang, L. Wei, A. Mahmood, C. Yan, J. Dong, S. Zhao and Y. Chen, *Matter*, 2020, **3**, 1442–1476.
41 H. Xu, D. Wang, P. Yang, L. Du, X. Lu, R. Li, L. Liu, J. Zhang and M. An, *Appl. Catal., B*, 2022, **305**, 121040.
42 Q. Zhang and J. Guan, *Energy Environ. Mater.*, 2021, **4**, 307–335.
43 J. Pampel and T.-P. Fellinger, *Adv. Energy Mater.*, 2016, **6**, 1502389.
44 Z. Shi, W. Yang, Y. Gu, T. Liao and Z. Sun, *Advanced Science*, 2020, **7**, 2001069.
45 C. Guo, R. Zhou, Z. Li, Y. Si, W. Liao, W. Sun, S. Xiang, X. Luo, M. Luo and Z. Luo, *Microporous Mesoporous Mater.*, 2020, **303**, 110281.
46 J. Yang, X. Feng, G. Lu, Y. Li, C. Mao, Z. Wen and W. Yuan, *Dalton Trans.*, 2018, **47**, 5065–5071.
47 D. Menga, F. Ruiz-Zepeda, L. Moriau, M. Šala, F. Wagner, B. Koyutürk, M. Bele, U. Petek, N. Hodnik, M. Gaberščček and T.-P. Fellinger, *Adv. Energy Mater.*, 2019, **9**, 1902412.
48 K. Ping, M. Alam, S. R. Kahnert, R. Bhadoria, A. Mere, V. Mikli, M. Käärik, J. Aruväli, P. Paiste, A. Kikas, V. Kisand, I. Järving, J. Leis, N. Kongi and P. Starkov, *Mater. Adv.*, 2021, **2**, 4009–4015.
49 M. Mazzucato, G. Daniel, A. Mehmood, T. Kosmala, G. Granozzi, A. Kucernak and C. Durante, *Appl. Catal., B*, 2021, **291**, 120068.
50 G.-L. Wen, H.-J. Niu, A.-J. Wang, Z.-Z. Yin, Q.-L. Zhang and J.-J. Feng, *J. Colloid Interface Sci.*, 2019, **556**, 352–359.
51 Y. Chen, Y. Huang, M. Xu, T. Asset, X. Yan, K. Artyushkova, M. Kodali, E. Murphy, A. Ly, X. Pan, I. V. Zenyuk and P. Atanassov, *Mater. Today*, 2022, **53**, 58–70.
52 C. Yang, W. Zhong, K. Shen, Q. Zhang, R. Zhao, H. Xiang, J. Wu, X. Li and N. Yang, *Adv. Energy Mater.*, 2022, **12**, 2200077.
53 P. Li, Y. Xuan, B. Jiang, S. Zhang and C. Xia, *Electrochem. Commun.*, 2022, **134**, 107188.
54 S. H. Lee, J. Kim, D. Y. Chung, J. M. Yoo, H. S. Lee, M. J. Kim, B. S. Mun, S. G. Kwon, Y.-E. Sung and T. Hyeon, *J. Am. Chem. Soc.*, 2019, **141**, 2035–2045.
55 C. Zhu, Q. Shi, B. Z. Xu, S. Fu, G. Wan, C. Yang, S. Yao, J. Song, H. Zhou, D. Du, S. P. Beckman, D. Su and Y. Lin, *Adv. Energy Mater.*, 2018, **8**, 1801956.
56 K. Chen, S. Kim, R. Rajendiran, K. Prabakar, G. Li, Z. Shi, C. Jeong, J. Kang and O. L. Li, *J. Colloid Interface Sci.*, 2021, **582**, 977–990.
57 M. Ishizaki, H. Tanno, H. Sutoh, T. Katsuki, T. Hayasaka, M. Yagi, Y. Tsubonouchi, K. Tajima, T. Kawamoto, Y. Sakuda and M. Kurihara, *ACS Appl. Energy Mater.*, 2020, **3**, 9040–9050.
58 K. Muuli, M. Mooste, S. Akula, V. Gudkova, M. Otsus, A. Kikas, J. Aruväli, A. Treshchalov, V. Kisand, A. Tamm, A. Krumme, S. Cavaliere and K. Tammeveski, *ChemElectroChem*, 2023, **10**, e202300131.
59 X. H. Li, W. L. Guo, Z. H. Liu, R. Q. Wang and H. Liu, *Appl. Surf. Sci.*, 2016, **369**, 130–136.
60 S. Fu, J. Song, C. Zhu, G.-L. Xu, K. Amine, C. Sun, X. Li, M. H. Engelhard, D. Du and Y. Lin, *Nano Energy*, 2018, **44**, 319–326.
61 V. Jose, J. M. V. Nsanzimana, H. Hu, J. Choi, X. Wang and J.-M. Lee, *Adv. Energy Mater.*, 2021, **11**, 2100157.

